Effect of vortex-injection interaction on wall heat transfer in a flat plate and fin corner geometry

By Juan R. LLOBET,[1)] Rowan J. GOLLAN[1)] and Ingo H. JAHN[1)]

[1)] *Centre for Hypersonics, University of Queensland, Queensland, Australia*

More flexible and economical access to space is achievable using hypersonic air-breathing propulsion. One of the main challenges for hypersonic air-breathing propulsion is reaching high combustion efficiency within the short residence time of the flow in the engine. Lengthening the combustor is not a viable option due to its many drawbacks, and the use of Hypermixers or strut injectors increase mixing efficiency at the cost increasing loses and heat load. On the contrary, inlet-generated vortices are an intrinsic feature of many scramjet inlets, and can be used to enhance mixing incurring minimal loses and heat load increase. A previous computational study used a canonical geometry consisting of a flat plate with a fin at different deflection angles to investigate the ability of inlet-generated vortices to enhance mixing rate. Significant increases in mixing rate were obtained due to the vortex-fuel plume interaction. The flow conditions were equivalent to those found in a Rectangular-to-Eliptical Shape Transition scramjet inlet at a Mach 12, 50 kPa constant dynamic pressure trajectory. Despite the minimal heat load increase of this approach, characterization of the vortex-fuel plume interaction effect on wall heat transfer is required. In this work the previous study is extended, describing the effect of the vortex-fuel plume interaction on wall heat transfer. Heat flux in the vicinity of the porthole injector reaches 200 % compared to the baseline case with no vortex interaction. Moreover, the injection bow shock affects the corner region, creating pockets of heat flux up to 75 % larger than the unaffected region. Additionally, the evolution of the fuel plume downstream of the injector location is investigated, describing the relationship between local maxima and minima of heat flux, and the location of the fuel on the wall surface. This relationship can be exploited in experimental data acquisition to obtain fuel location from heat flux data. The viability of this experimental approach is explored using computational data, confirming that through careful sensor placement position measurements with an accuracy higher than ±5 mm can be achieved.

Key Words: Scramjet, Heat flux, Vortex-injection interaction, Injection, Vortex

Introduction

Air-breathing engines, contrary to rocket engines, are not required to carry oxidizer. This fact grants scramjets a theoretically higher specific impulse than rocket engines. This can lead to gains in payload mass fraction and efficiency.[1,2)] Nonetheless, scramjet engine development still requires a solution to several technological obstacles. Amongst these, efficient and fast air-fuel mixing, as well as heat transfer management in the inlet and combustor are key problems. The flow in a scramjet is decelerated and compressed across the inlet. The compression ratio is a compromise between efficient and robust combustion and structural and thermal load management, amongst other considerations.[3)] The levels of pressure and temperature reached at high Mach number flight require advanced materials and careful design of wall cooling systems.[4,5)] Therefore, detailed knowledge of the heat load across the engine is required to efficiently design the heat management system. Moreover, despite the deceleration performed in the inlet, supersonic speeds are preserved along the total length of the engine. This hinders mixing efficiency, as it leads to very short residence times in which the fuel has to be injected, mixed and burned. Increasing the residence time by lengthening the combustor is an impractical solution, as the combustor is a major contributor to the total engine heat losses, and total drag.[6,7)] In addition, the use of mixing enhancement devices, such as hypermixers or struts, can incur significant additional drag and heat load issues.[7,8)] Hence, high interest lies in solutions for increasing fuel mixing rate that generate minimal additional losses and heat loads. A possible approach is to use vortices present in the flowfield to enhance mixing. Non-axisymmetric scramjet engines inherently generate vortices due to shock-wave boundary-layer interactions.[9)] These flow features are present in the flow intrinsically. Therefore, any improvement in mixing rate comes at little or no additional loses. The potential of these vortices for mixing enhancement by vortex-injection interaction has been shown previously.[10)] Mixing rates up to 870 % higher than those found in the case of injection on a flat plate were shown. The vortex-injection interaction was found to increase mixing through multiple mechanisms. The most significant mechanism is the fuel plume distortion which increases the effective surface for air-fuel mixing. However, this distortion also modifies the fuel distribution and the shock-wave pattern surrounding the fuel plume, altering the heat flux downstream of the injector. Scramjet combustors are subject to very high heat loads, which makes thermal load management critical to the viability of future scramjets.[11)] Therefore, detailed knowledge of zones with localized heating and high temperature gradients such as the vicinity of porthole injector and corner regions is of great importance, as it affects the choice of thermal management system and materials.[12)] The present work studies the effect of the vortex-injection interaction on wall heat flux distribution (Q_w) in a scramjet representative geometry. In addition, the relationship between the location of the fuel on the surface and the heat flux distribution is investigated.

Vortex generation

In non-axisymmetric scramjet inlets, shock-shock and shock-viscous interactions generate streamwise vortices. It has been shown[9,10,13] that a simplified inlet-like geometry can be used to generate a flowfield and vortices equivalent to those formed by scramjet inlets. This geometry is a flat plate and a fin positioned at an angle relative to the flow. In this study three deflection angles for the fin $\left(\alpha_{fin}\right)$, 5°, 10° and 15°, are used. Fig. 1a shows the $\alpha_{fin} = 10°$ geometry together with the most relevant flow features. The flat plate extends upstream of the fin leading edge, allowing for boundary layer growth. The fin generates an oblique shock that interacts with the flat plate boundary layer. As described in previous works,[9,10,13] the low velocity in the viscous region over the flat plate allows the shock-processed high-pressure flow to be convected spanwise towards the low pressure region. This crosswise flow causes the roll up and detachment of the boundary layer that generates the vortex, as depicted in Fig. 1b. This figure shows velocity contours in the vortex region for the case with $\alpha_{fin} = 10$, on a plane 100 mm downstream of the fin leading edge. The solid line (δ) indicates the boundary layer edge, defined as the line with 95 % of the freestream total enthalpy. The discontinuous lines are a depiction of the vortex description by Alvi and Settles.[9] The crosswise flow is fed by flow from the upper region behind the fin shock, as depicted in Fig. 1b marked as *Jet*. The flowfield exhibits a quasi-conical behaviour about the fin leading edge.[13] This means the flow structure is preserved in the axial direction starting slightly downstream of the fin leading edge, once the flowfield is established. The flow features scale linearly with the axial direction. Thus, the flow is visualized as constant in the streamwise direction using the normalize coordinates (Y/X) and (Z/X). This fact is exploited to describe the vortex flowfield using conical coordinates in Fig. 1b.

Computational approach

Computational Fluid Dynamics (CFD) simulations are performed on the flat plate and fin geometry with a porthole injector placed on the flat plate 100 mm downstream of the fin leading edge. Two locations are used for the porthole injector. The first one is located in the vicinity of the separation line. The second one is located coincident with the normal projection of the vortex core on the flat plate.[10] These will be referred as *separation* (S.i.) and *core* (C.i.) injection, and are marked in Fig. 1b as S.i. and C.i. respectively. Moreover, three different deflection angles are used for the fin: $\alpha_{fin} = 5°$, 10° and 15°. Hydrogen (H_2) is used as fuel, injected in a mixture of 92 % air and 8 % Nitric Oxide (NO) mass fraction (NO added to match future ground test experiments). Two different injection-to-freestream-momentum flux ratios $\left(J = \left(\rho u^2\right)_{inj} / \left(\rho u^2\right)_{\infty}\right)$, $J = 1$ and $J = 3$ are used. The simulated plenum pressures are 0.430 MPa and 1.3 MPa respectively, both with a total temperature of 300 K. The porthole injector is inclined 45° in the axial direction and its diameter is 1.0 mm. In order to obtain data relevant to real scramjet operation, the flow conditions represent those found in the MACH 12 REST engine[14,15] tested at a 50 kPa constant dynamic pressure trajectory operating condition.[16] Barth et al.[16] present a complete investigation of the flowfield, from which the values of velocity (U), dynamic pressure (q), and total enthalpy (H_0) summarized in Table1 have been extracted.

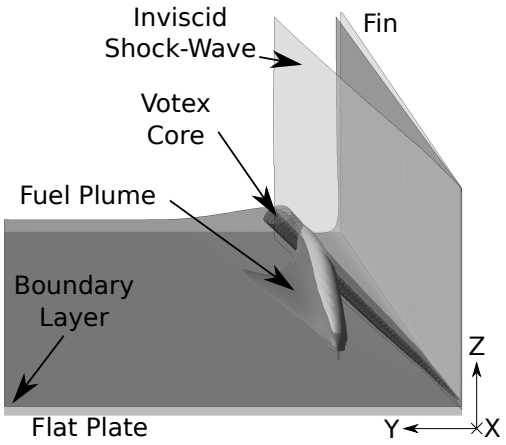

(a) Vortex formation and fuel plume

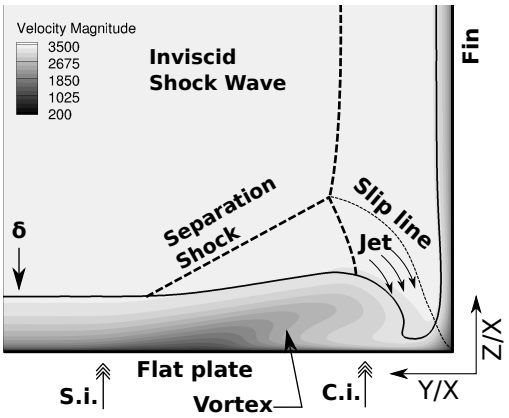

(b) Vortex flowfield structure. δ and contours from $\alpha_{fin} = 10$ case. Discontinuous lines are adapted from Alvi and Settles[9]

Fig. 1.: Test geometry and vortex flowfield structure depiction.

	Mach No.	U	q	H_0
Inflow	7.3	3471 m s^{-1}	161.0 kPa	6.5 MJ kg^{-1}

Table 1.: Flow conditions

The US3D code developed at the University of Minnesota[17] is used as CFD solver. Non-reacting steady-state RANS simulations using the SST turbulence model with a Schmidt number (Sc) of 0.7 are performed. Wall boundaries are at a constant temperature of 300 K, to match future cold wall ground-test experiments. Convective fluxes are calculated using the Steger-Warming flux vector splitting method. The MUSCL scheme with pressure limiter is used in zones of strong shocks. The DPLR method[18] is used for the implicit time integration. Varying CFL numbers are used throughout the calculation, with a value of 50 for the final time steps.

The numerical domain includes a 300 mm long 200 mm wide flat plate and a 100 mm high fin with an infinitely sharp leading edge. The fluid domain starts 10 mm upstream of the fin leading edge. The fin extends to the downstream end of the fluid domain. A non-uniform inlet profile is prescribed at the upstream boundary. The profile was obtained in a separate simulation and

represents the boundary layer developed over a 250 mm long flat plate, resulting in a thickness of 6.5 mm. A grid independence analysis was performed based on the most relevant parameters, such as mixing efficiency, penetration, and fuel plume shape, demonstrating that the solutions were mesh independent. The grids used for the different cases range between 3.7 and 3.9 million cell. Extensive study was conducted to verify the US3D predictions of the heat flux using the SST $k-\omega$ model for different y^+ values (Will Landsberg, personal communication, 23 March , 2016), showing little variation in the result for this turbulence model below $y^+ = 1$. The current work uses a typical near-wall cell size of 2 µm, keeping the y^+ value below 1. Halving the first cell height yielded heat flux results with less than 1.4 % difference in the region of interest.

Heat flux distribution

The heat flux distribution generated by the cases of injection in the separation line S.i. and in the vortex core C.i. are presented in this section. As described in previous works,[10] the fuel plume is distorted by the influence of the vortex. The region of the plume adjacent to the flat plate is subject to an intense crosswise flow. Therefore, this region is strongly convected in the spanwise direction. However, the effect of the vortex on the upper region of the plume is much smaller, and this region follows the freestream velocity. This effect can be observed in Fig. 2, where contours of heat flux on the flat plate, along with slices across the fuel plume depicting contours of H_2 mass fraction (csH_2) are shown. The distortion of the fuel plume affects the fuel distribution on the surface of the flat plate, as well as the shock structure around the injection region. This modifies the heat flux pattern downstream of the injector, changing the locations of high and low heat flux regions. The interaction between the vortex, the fuel plume and the incoming freestream plays an important role in the heat transfer distribution on the flat plate and the fin. To understand the relationship between the fuel plume region in contact with the wall and the heat flux contours, the flow around the fuel plume is inspected.

Heat flux in the injector vicinity A strong variation in heat flux in the region adjacent to the porthole injector is visible in Fig. 2 for both cases. The fuel, with a total temperature of 300 K, expands during the injection process reaching temperatures as low as 55 K in the coldest region. The axial velocity of the fuel jet is significantly lower than the velocity of the freestream, producing a region of low velocity which reduces heat transfer coefficient. The low temperature of the plume and low velocities generate a substantial drop in heat flux around and just downstream of the porthole. The region just downstream of the bow shock presents the highest values of heat flux. Fig. 3a includes the maximum values of heat flux downstream of the injection bow shock for the S.i. and C.i. cases, as well as the case of injection in a flat plate (*FP.i.*) (injection without vortex interaction). The flow conditions in the separation line are similar to those of the undisturbed flow. Therefore, the Separation injection cases show values of heat transfer very similar to the case with no vortex interaction. However, two effects due to the proximity of the separation line modify the maximum heat flux values: flow deflection and thickening of the boundary layer.

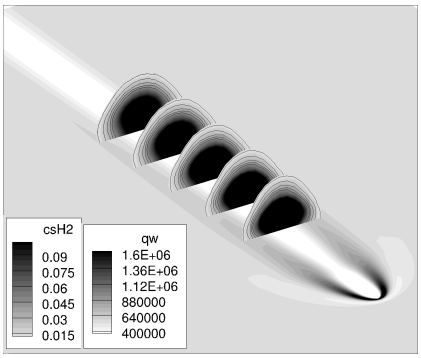

(a) Flat plate injection, $J = 1$.

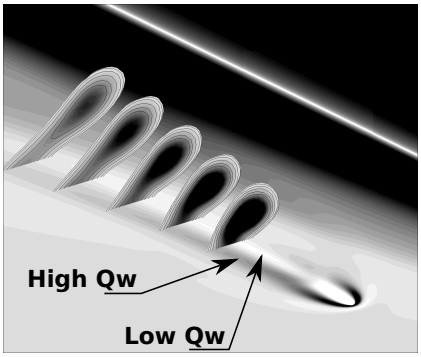

(b) Separation injection, $J = 1$, $\alpha_{fin} = 10°$.

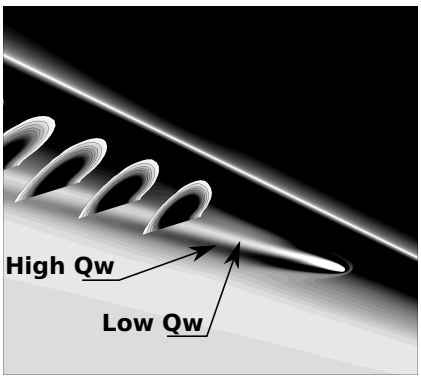

(c) Core injection, $J = 1$, $\alpha_{fin} = 10°$.

Fig. 2.: Wall heat flux and fuel plume H2 mass fraction contours

The subsonic conditions in the boundary layer allow information to travel upstream. This causes the flow in the boundary layer to deflect a short distance upstream of the separation line, as indicated in Fig. 4a. Therefore, the flow impinges on the fuel jet with a tangential component. This increases the effective injector angle (45° in the axial direction) seen by the flow. This increases the strength of the injection bow shock, generating the higher heat transfer observed in the Separation cases compared to the flat plate injection. In addition, the adverse pressure gradient that separates the flow also produces a thickening of the boundary layer immediately upstream of the separation line. The thickening of the boundary layer reduces the maximum heat flux near the injector by reducing the heat transfer coefficient of the incoming flow. This thickening is more severe for higher adverse pressure gradients. Thus, higher fin angles produce thicker boundary layers in the vicinity of the porthole, reducing heat transfer coefficient further. This is responsible for the reduction in heat flux with increasing fin angle in the

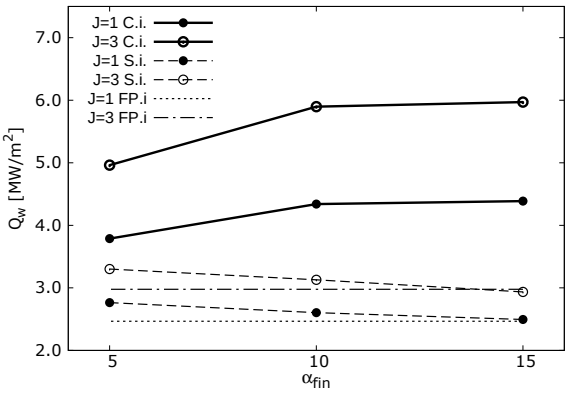

(a) Porthole region

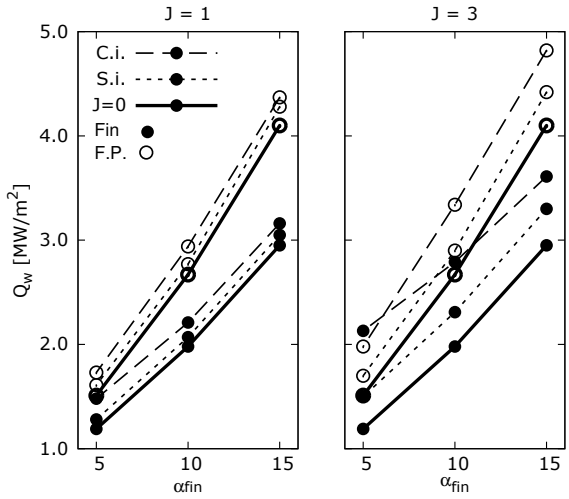

(b) Fin and flat plate corner region. Solid dots indicate Fin, hollow indicate flat plate.

Fig. 3.: Maximum heat flux in the porthole and fin-flat plate corner

vicinity of the porthole injector seen in Fig. 3a. The flow deflection and reduction in heat flux near the separation line can be observed in Fig. 4a.

The porthole injector in the core injection cases C.i. is placed in the region of flow affected by the fin shock wave. Therefore, this area presents high heat flux values, which are further increased just upstream of the injector by the injection bow shock. Increasing fin angles increase the heat flux surrounding the injector. Thus, the maximum heat flux value near the injector could be expected to increase accordingly. However, increasing fin angle increases dynamic pressure, reducing the effective injection-to-freestream momentum flux ratio. Moreover, the Mach number in this region is also reduced. Both effects weaken the bow shock. As a result, maximum heat flux behind the bow shock tends to plateau with increasing fin angle, as seen in Fig. 3a.

Heat flux downstream from the injector Downstream from the injector, two distinct areas with high and low heat flux values can be identified. These are highlighted in Fig. 2. The heat flux Q_w contours in Fig. 4 show the extent of the affected heat flux zone. This region extends up to 100 mm downstream of the injector location.

For the case of the injector on a flat plate, the region of low heat flux follows the region of high fuel concentration. This can be observed in Fig. 2a. The regions of high concentration of fuel mass fraction csH_2 near the wall correspond to the region of low heat flux Q_w. These regions are bounded by regions of high heat flux, as the flow processed by the injector bow shock is convected downstream surrounding the fuel plume. The C.i. case shows a similar behaviour, with the regions of low heat flux located immediately below the regions of high fuel concentration in the plume, as can be see in Fig. 2c. However, for the S.i. case, the plume region on the flat plate surface aligns with the boundary between high and low heat flux areas, as can be seen in Fig. 2b. This is explained by the distortion of the fuel plume due to the vortex interaction, and the velocity profile within the vortex region. As observed in Fig. 1b, the detached boundary layer rolls up in the vortex core, generating a thick region of slow flow. The crosswise flow in the vortex pushes the lower region of the core towards the separation line. Thus, in the S.i. cases, the fuel plume side closer to the fin is met by the flow coming from the vortex core region. On the other hand, the plume side further from the fin is in contact with the thin boundary layer of the undisturbed freestream. As the fuel mixes with the surrounding flow, the different conditions in both sides generate a velocity gradient across the two sides of the fuel plume. The thick boundary layer in the region closer to the fin decreases the heat transfer coefficient, decreasing the heat flux in comparison with the opposite side of the plume. This fact can be observed in Fig. 4, where contours of heat flux and wall shear stress (τ_{wall}) are compared. The enlarged detail plots show wall shear stress iso-lines superimposed to the heat flux contours. The wall shear stress and heat flux contours correlate very closely. This shows that the main parameter affecting heat flux is the change in heat transfer coefficient across the region of fuel on the flat plate surface.

Heat flux in the corner region Further from the injector, the effect of the injection bow shock on heat flux is especially relevant near the corner. As can be seen in Fig. 4 and 5, the baseline heat flux in the corner region is higher than in the rest of the model due to the effect of the fin shock. The heat flux value on the flat plate downstream of the fin shock is slightly higher than on the fin surface due to the effect of the crosswise and *jet* flows. As previously described,[9,10,13] the flow processed by the fin shock flows towards the flat plate feeding the crosswise flow. This flow, previously heated by the fin shock and viscous effects near the fin wall, impinges on the flat plate increasing the heat flux. When the injection bow shock reaches the corner walls, it increases the heat flux even further. To visualize the bow shock location, regions of density gradient maxima in the direction of the velocity $\left(d^2\rho/dn^2 = 0\right)$, with a filter based on gradient density ($d\rho/dn > \epsilon$) can be used.[19] The standard approach for extracting shock surfaces from the flowfield cannot be used on a non-slip surface. Moreover, in regions of subsonic flow shock waves do not exist. Nonetheless, Eq. 2 is used to obtain regions of density gradient maxima on the surface, indicating the regions affected by the shock near the wall. In this equation, the direction of the velocity ($v/|v|$) is substituted by the direction of the wall shear stress ($\tau/|\tau|$). The lines of maximum density gradient, bold lines in Figs. 4 and 5 have been obtained

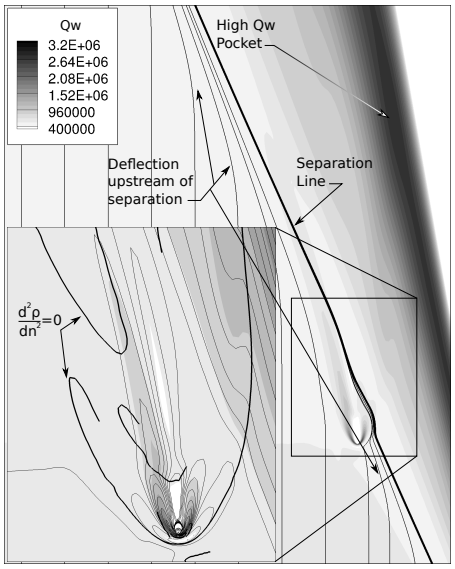

(a) Separation injection, $J = 1$, $\alpha_{fin} = 10°$.

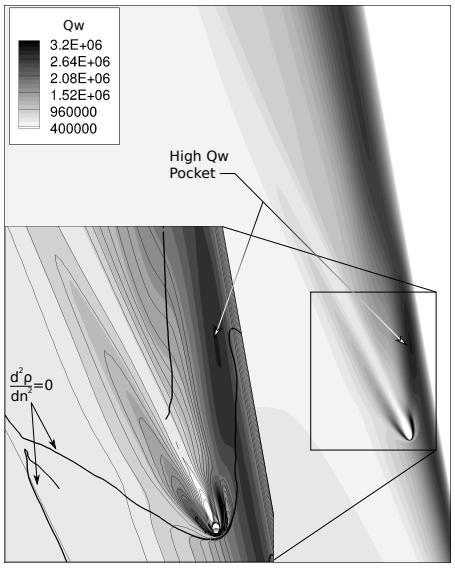

(b) Core injection, $J = 1$, $\alpha_{fin} = 10°$.

Fig. 4.: Plan view of heat flux contours, including separation line and streak lines in figure (a). Magnified sections show: contours of heat flux, iso-lines of wall shear stress and line of $\frac{d^2\rho}{dn^2} = 0$ (bold line).

with Eq. 1, setting the gradient filter as per Eq. 2.

$$\text{Shock line: } \frac{d^2\rho}{dn^2} = \nabla\left(\nabla\rho \cdot \frac{\tau}{|\tau|}\right) \cdot \frac{\tau}{|\tau|} = 0 \tag{1}$$

$$\text{filter: } \frac{d\rho}{dn} = \nabla\rho \cdot \frac{\tau}{|\tau|} > 0.2 \tag{2}$$

In Fig. 4b, pockets of high heat flux generated by the injection bow shock can be observed on the flat plate surface near the fin wall, just behind the line of $d^2\rho/dn^2 = 0$. In Fig. 4a this pocket takes place further downstream and it is not visible in the magnified section, although it can be faintly observed in the plan view. On the fin surface, the effect of the bow shock is equivalent to the effect on the flat plate. The high heat flux pockets on the fin can be observed in Fig. 5, where contours of heat flux and lines of $d^2\rho/dn^2 = 0$ are depicted.

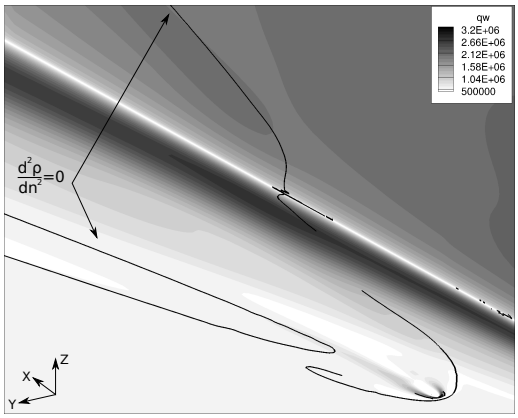

(a) Separation injection, $J = 1$, $\alpha_{fin} = 10°$.

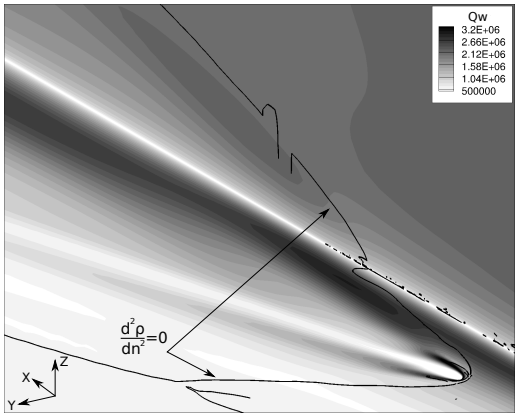

(b) Core injection, $J = 1$, $\alpha_{fin} = 10°$.

Fig. 5.: Heat flux contours and regions of $\frac{d^2\rho}{dn} = 0$.

To compare the effect of the bow shock on each case, the maximum values of wall heat flux on the fin and flat plate corner region are plotted in Fig. 3b. For equal injection momentum, the core injection cases C.i. show higher values of maximum heat flux than the separation injection cases due to the proximity of the injector to the walls. For each injector location, higher injection-to-freestream-momentum flux ratio J generate higher maxima due to the stronger injection bow shock. Additionally, it can be observed that the increase in heat flux is higher on the flat plate surface rather than on the fin, except for the $\alpha_{fin} = 5°$ $J = 3$ case. For all cases except this one, the high heat flux pocket on the flat plate appears significantly closer to the injector location than the pocket on the fin surface. This can be observed in Fig. 5 for the $\alpha_{fin} = 10°$ $J = 1$ case. The higher strength of the bow shock closer to the injector contributes to the higher heat flux values on the flat plate. In the $\alpha_{fin} = 5°$ $J = 3$ case, the proximity of the injector to the fin, the shallow fin angle, and the high value of J allow the bow shock to impinge on the fin relatively close to the injector, resulting in a heat flux value on the fin slightly higher than on the flat plate surface.

Heat flux as indicator of surface fuel location

To quantify the evolution of the heat transfer across the plume region, values of heat flux Q_w, and Hydrogen mass fraction csH_2 at the wall have been extracted at a range of axial locations. The axial distances (X_i) are measured from the injector location. Corresponding lines at three axial locations are plotted

in Fig. 6. The low Y/X regions show high heat flux Q_w values, corresponding with the flow processed by the fin shock. The heat flux values for the three lines are coincident in the regions unaffected by the injection, as the flow in those areas follows the quasi-conical behaviour. The zones of high H_2 concentration indicate the location of the fuel on the wall surface. The peaks and valleys in heat flux show the zones affected by the injection. A local maximum and a local minimum are clearly noticeable for each line. The location of the higher concentration of H_2, and the location of the local maxima and minima of heat flux Q_w are related. In the S.i. case shown in Fig. 6a, the peak in fuel concentration coincides with the halfway point between the maximum and minimum in wall heat flux, and most of the fuel is located between the two. In the C.i. case, the peak in fuel concentration coincides with the local minimum of Q_w, with the local maxima indicating the limit of the zone of high H_2 mass fraction. This correlation between fuel location and heat flux can have important implications for controlling and predicting heat loads near scramjet corner or swept separation streamwise vortices. In addition, this relationship between heat flux and fuel concentration enables a new experimental approach. Well-established heat transfer measurements, which are ideal for shock tunnel tests, can be used to determine the location of fuel plumes.

As the fuel on the wall is convected downstream, the effect of the plume on heat flux is reduced. After about 50-70 injector diameter lengths downstream of the injector, it is impossible to obtain the fuel location on the surface from heat flux measurements. However, another property of the vortex-injection interaction can be used to estimate this location. As the fuel is convected downstream, the plume converges to a quasi-conical behaviour. In Fig. 6a, the evolution for the S.i., $\alpha_{fin} = 10$, $J = 1$ case is presented. With increasing X_i axial coordinate, the H_2 mass fraction peak location converges to a constant value of Y/X, meaning it is following the quasi-conical flow. In Fig. 7, the plume location evolution for the S.i. and C.i. cases is compared. This figure shows the difference in H_2 concentration for both cases due to the different penetration for the two injector locations.[10] Most importantly, it shows that the surface fuel in both plumes converge to the same location. In the $\alpha_{fin} = 10$ case the separation line sits at $Y/X = 0.44$. Thus, Fig. 7 indicates that the flow on the surface is convected to just within the separation region, adjacent to the separation line. This can be explained by the effect of the crosswise flow and the separation of the freestream. The surface fuel on the separated region is convected towards the separation line by the crosswise flow. On the other hand, the surface fuel outside of the separation region reaching the separation line is convected upwards following the separated freestream, moving the fuel from the surface towards the bulk of the flow in the core region. The injection in the S.i. cases take place a few millimetres outside of the separation line (6.3 mm in the $\alpha_{fin} = 10°$ $J = 1$ case). In this case the fuel on the wall surface is convected from higher to lower Y/X towards the separation line, crossing it until all fuel on the surface is on the fin side of the separation. In the same fashion, the fuel on the wall surface coming from the core region injector is convected by the flow moving away from the fin. In this case moving from low to high Y/X until it approaches the separation line.

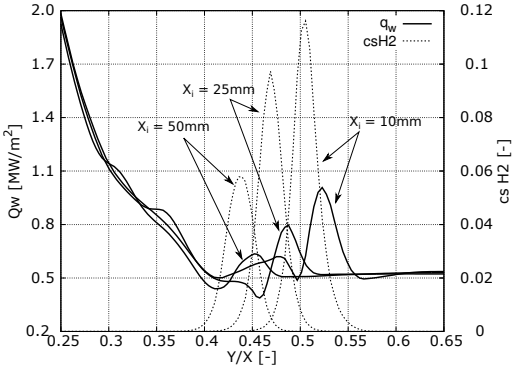

(a) Separation injection, $J = 1$, $\alpha_{fin} = 10°$.

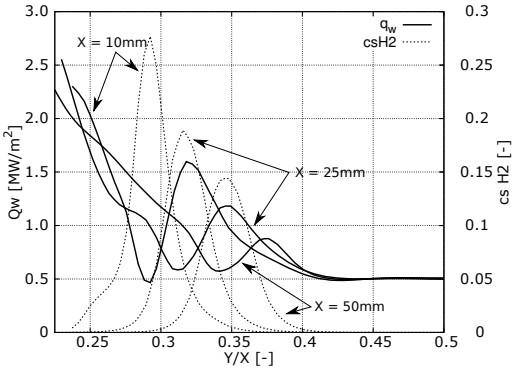

(b) Core injection, $J = 1$, $\alpha_{fin} = 10°$.

Fig. 6.: Flat plate Q_w and csH_2 at $X_i = 10$, 25 and 50mm.

CFD to inform heat transfer gauge placement

Obtaining heat flux experimental data on the vortex-injection interaction process will serve to validate the results obtained in this computational investigation. Moreover, obtaining the location of the fuel on the wall surface experimentally provides valuable data for validation of previous works focused on mixing and fuel distribution.[10] The viability of using heat transfer measurements for tracking the fuel over the flat plate in an experimental model is investigated using CFD. In the experiment, a series of heat transfer gauges will be placed at lines of constant X_i as depicted in Fig. 8a, to obtain results equivalent to those shown in Fig. 6a.

In the experimental testing, the number of heat transfer gauges and maximum resolution are limited. Thus, careful selection of the placement of the gauges is required to accurately retrieve the location of maximum and minimum heat transfer Q_w. To study the effect of gauge distribution on the ability to reconstruct the heat transfer profile and fuel distribution, a numerical experiment was conducted using data from the S.i., $\alpha_{fin} = 10$, $J = 1$ case presented above. Numerical heat transfer gauges with a surface cross-section 2 mm × 0.3 mm, located at lines of constant X_i, were added to the simulation. The gauges are oriented parallel to the axial direction, which provides better spatial resolution in the spanwise direction. The number of extraction points (gauges) is varied between 5 to 30 per line (80 to 480 gauges per meter approximately). The separation between extraction points is constant, and the distance from the first gauge to the fin (Y_0) is the same for all lines. For each measurement, the value at each gauge is used to fit a curve us-

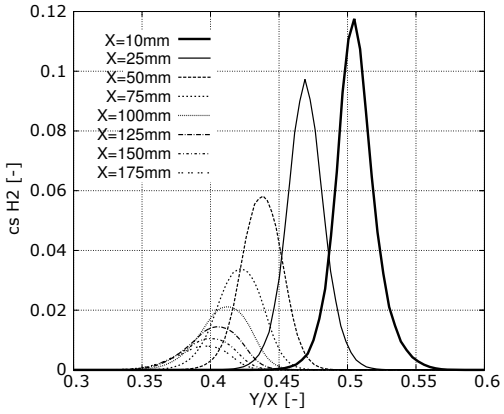

(a) Separation injection, $J = 1$, $\alpha_{fin} = 10°$.

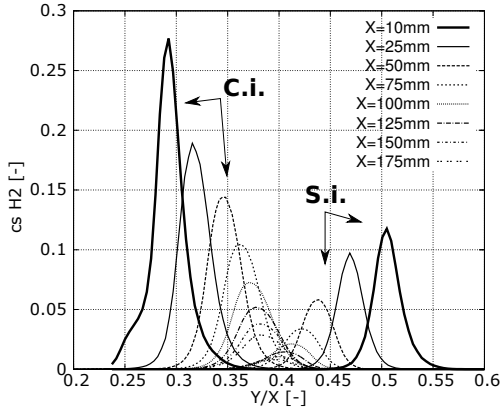

(b) Separation and Core injection, $J = 1$, $\alpha_{fin} = 10°$.

Fig. 7.: csH_2 evolution with increasing X_i.

ing a shape-preserving piecewise cubic interpolation.[20] The fitted curve is then analysed to obtain the locations of the local maximum and minimum values of heat transfer. To account for experimental uncertainty, a perturbation with a normal random distribution was applied to each gauge measurement. Previous experimental work[21] with equivalent flow conditions found an experimental uncertainty for flat plate measurements of approximately 10 % of the measurement value. The normal distribution for the perturbation was modelled assuming a mean value (μ) equal to the CFD value at the gauge location. The standard deviation (σ) value was selected to simulate the uncertainty level of 10 %, ($2 \cdot \sigma = 10\,\%\mu$). To simulate the effects of experimental error and measurement uncertainty on data interpretation, a Monte-Carlo simulation was conducted. 100 sample experiments each with a different random perturbation of the measurements were performed, resulting in 100 different curve fits to the same original data. By analysing each curve to find the location of the local maximum and minimum heat flux Q_w, and analysing the resulting distribution of position, the accuracy of the method is established.

In addition to the measurement uncertainty, the flow conditions in the experimental facility are also subjected to experimental variations. These can slightly modify the shock angles and alter the vortex and plume locations. Thus, the relative location of the gauges with respect to the plume is unknown a priori. The relative location of the gauges and the local maximum and minimum of heat flux can affect the accuracy of the curve fitting. In order to account for the sensitivity of the fitted data on the relative position of fuel plume and gauges, a number of extractions (N) are performed with modified gauge spanwise location. The distance between gauges $\left(\Delta_g\right)$ is maintained in each of the extractions, but the distance between the first gauge and the fin wall is altered. The offset value is calculated as $\Delta_g / (N-1)$ in order to sweep the distance between gauges. This process is depicted in Fig. 8b, where Y_0 is the Y coordinate for the first gauge and X_i is the axial coordinate from the fin leading edge of the line of gauges. $N = 10$ is used in this study. Fig. 9 shows the reconstructed location of the local maxima and minima, as function of the gauge density (gauges/m). For each value of gauge density, the mean location (solid line) is calculated by averaging the values obtained for all the different Y_0 offsets. Also shown are 95 % confidence intervals as grey bands. These bands signify the $\pm 2\sigma$ region of the reconstructed locations from the Monte Carlo study. The dashed horizontal lines represent the target values, obtained from the CFD calculation. The error of the reconstructed locations is plotted in Fig. 10. Different trends in the error are shown for the location of the maximum and minimum. The line at $X_i = 0.01$ m shows better accuracy for the location of local maximum heat transfer than the lines situated further downstream. However, the opposite occurs for the local minimum heat transfer location. As observed in Fig. 6a, the maximum heat transfer at $X_i = 0.01$ m has a relatively high and wide peak. On the contrary, the local minimum for the $X_i = 0.01$ m line is located in a relatively narrow valley, requiring higher gauge density to reach accurate retrieval of its exact location. Looking back at Fig. 6a, it can be seen that close to the injector the heat transfer flux distributions have large and well defined minima and maxima, allowing high reconstruction accuracy. This is visible in Fig. 9, where

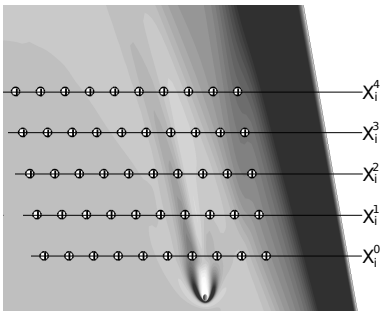

(a) Proposed location of gauges for experimental testing

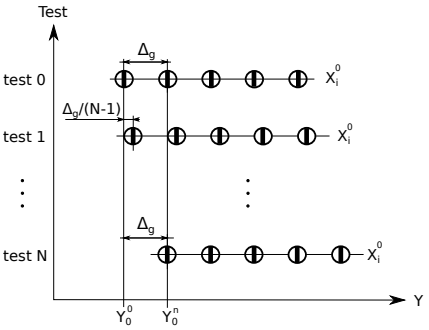

(b) Gauges offset sketch

Fig. 8.: Gauges distribution.

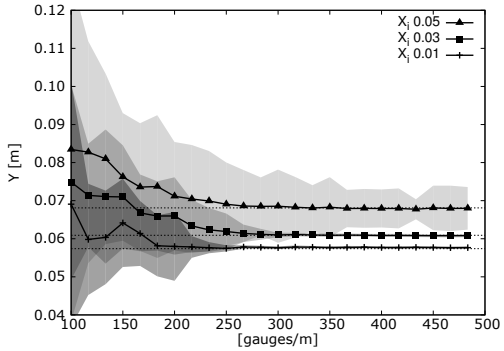

(a) Local maximum

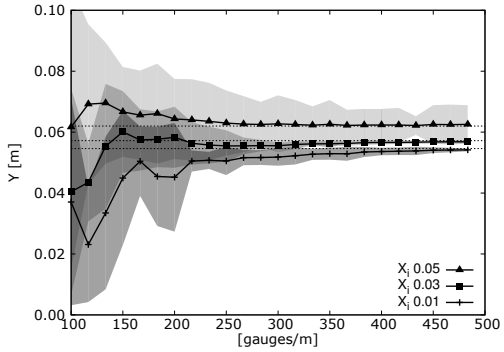

(b) Local minimum

Fig. 9.: Averaged position of the heat flux local maximum and minimum including 95% confidence range.

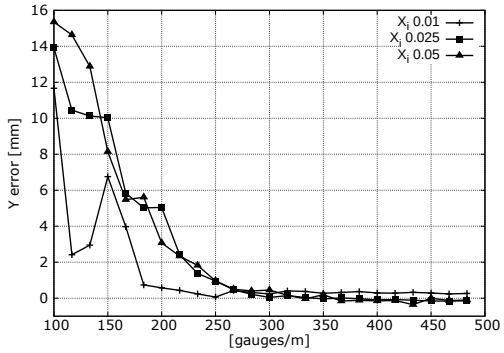

(a) Local maximum

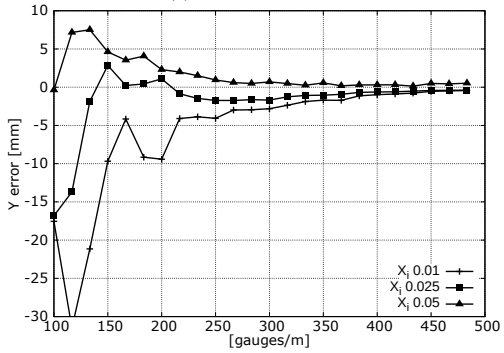

(b) Local minimum

Fig. 10.: Error of averaged heat flux local maximum and minimum location.

the 95 % confidence range for the $X_i = 0.01$ m and $X_i = 0.03$ m reaches a negligible value above 300 gauges/m. As the distance from the injector increases, the effect of the plume on wall heat transfer, Q_w weakens, producing lower peaks. This reduces the reconstruction accuracy. This can be observed in the $X_i = 0.05$ m line, for which the uncertainty remains relatively high for all gauge densities. Further from the injector location, the Q_w peaks are of the order of the artificially introduced experimental noise. This highly hinders the reconstruction of peak position, rendering it impossible when the peaks amplitude is masked by experimental noise.

For the present case, a density of 250 gauges/meter is considered a good compromise. The number of gauges is manageable in an experimental set-up and the error for the location of local maxima and minima remains at less than ±5 mm at all key locations, although the uncertainty for the $X_i = 0.05$ m is relatively high.

Fig. 11 has been obtained applying this approach on the cases with the different fin angles (5°, 10° and 15°) and injection location (S.i. and C.i.). In the figure, each dot type represents a combination of α_{fin} and injector location. The solid/dashed line and solid/hollow dot combination represent the axial location of the gauges line. This figure confirms that an experimental set up with 250 gauges/meter produces satisfactory results for most of the cases and axial location of the gauges line.

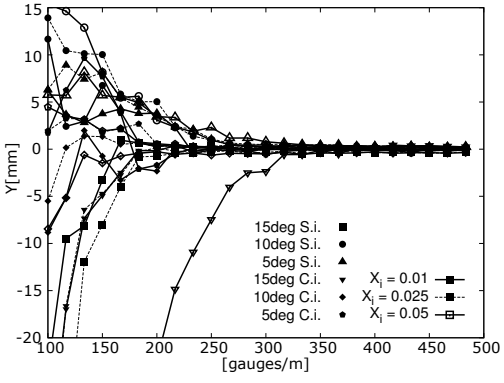

(a) Local maximum

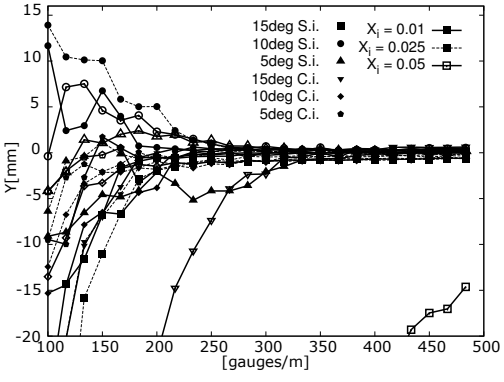

(b) Local minimum

Fig. 11.: Average error for the cases with $J = 1$.

Conclusions

A flat plate with a fin at a deflection angle has been used to generate vortices and to study the effect of the vortex-injection interaction on heat transfer. Data from cases with three different fin deflection angles, two injector locations and two injection-to-freestream momentum flux ratios are presented. The locations of increased heat flux due to the injection process have been identified and described. For all cases maximum heat flux to the flat plate occurs just upstream from the injector. The highest heat fluxes, up to 200 % larger than the injection in a flat

plate where obtained for the injection in the core region. This increase plateaus with increasing fin deflection angle. Furthermore, further away from the injector, the impingement of the injection bow shock on the flat plate and fin generate pockets of increased heat flux, with values up to 75 % larger than the unaffected regions. This work also showed that heat flux on the flat plate are generally higher than on the fin. Far downstream from the injector, the fuel on the wall surface aligns with the location of the separation line. Zones of local maxima and minima in the heat transfer have been identified, and linked to the fuel distribution on the surface. This allows inference of the location of the fuel on the wall surface from heat flux measurements.

Moreover, a numerical experiment has been conducted to assess the viability of using thin film gauges to reconstruct the heat flux Q_w profiles and to retrieve the location of the fuel on the flat plate surface experimentally. A preliminary investigation on the density of gauges required was performed. For the test case selected for the investigation, a minimum accuracy of 5 mm for the location of the local maxima and minima in heat transfer profile can be obtained using a gauge to gauge separation of 4 mm. This gauge to gauge separation is shown to perform satisfactorily for most of the presented cases.

References

1) Smart, M. K. & Tetlow, M. R., *Orbital delivery of small payloads using hypersonic airbreathing propulsion*, J. Spacecraft Rockets, 46, No.1, 2009, 117-125.
2) Cook, S. & Hueter, U., *NASA's integrated space transportation plan 3rd generation reusable launch vehicle technology update*, Acta Astronautica, 53, 2003, 719-728.
3) Smart, M. K., *How Much Compression Should a Scramjet Inlet Do?*, AIAA Journal, 50, No.3, 2012, 610-619.
4) Morgan, R. G. & Stalker R. J., *Shock Tunnel Measurements of Heat Transfer in a Model Scramjet*, Journal of Spacecraft and Rockets, 23, No.5, 1986, 470-475.
5) Zander, F. & Morgan, R. G., *Transient Heat Analysis of a Carbon Composite Scramjet Combustion Chamber*, 16th Australasian Fluid Mechanic Conference, 2007, Gold Coast, Australia, 1177-1181.
6) Paul, A., Stalker, R. J. & Mee, D. J., *Experiments on supersonic combustion ramjet propulsion in a shock tunnel*, Journal of Fluid Mechanics, 296, 1995, 159-183.
7) Fuller, R. P., Wu, P. K., Nejad, A. S. & Schetz, J. A., *Comparison of physical and aerodynamic ramps as fuel injectors in supersonic flow*, *J. Propul. Power*, 14, No.2, 1998, 135-145.
8) Fureby, C., Nordin-Bates, K., Petterson, K., Bresson, A. & Sabelnikov, V.,*A computational study of supersonic combustion in strut injector and hypermixer flow fields*, Proceedings for the Combustion Institute, No.35, 2015, 2127-2135.
9) Alvi, F. S. & Settles, G. S., *Physical model of the swept shock wave/boundary-layer interaction flowfield*, AIAA Journal, 30, No.9, 1992, 2252-2258.
10) Llobet, J. R., Jahn, I. H. & Gollan, R. J., *Effect of Streamwise Vortices on Scramjets Porthole Injection Mixing*, Proceedings for the 20th AIAA International Space Planes and Hypersonic Systems and Technologies Conference, Glasgow 2015.
11) Daniau, E. & Bouchez, M. & Herbinet, O. & Marquaire, P. M. & Gascoing, N. & Gillard, P., *Fuel reforming for scramjet thermal management and combustion optimization*, AIAA/CIRA 13th International Space Planes and Hypersonics Systems and Technologies Conference, 2005, Italy, 3, 1799-1807.
12) Glass, D. E.,*Ceramic Matrix Composite (CMC) Thermal Protection Systems (TPS) and Hot Structures for Hypersonic Vehicles*, 15th AIAA International Space Planes and Hypersonic Systems and Technologies Conference, Reston, VA, 2008; AIAA-2008-2682.
13) Kubota, H. & Stollery, J. L., *An experimental study of the interaction between a glancing shock wave and a turbulent boundary layer*, Journal of Fluid Mechanics, 116, 1982, 431-458.
14) Smart, M. K., *Design of three-dimensional hypersonic inlets with rectangular-to-elliptical shape transition*, Journal of Propulsion and Power, 15, No.3, 1999, 408-416.
15) Smart, M. K., & Trexler, C. A., *Mach 4 performance of hypersonic inlet with rectangular-to-elliptical shape transition*, Journal of Propulsion and Power, 20, No.2, 2004, 288-293.
16) Barth, J. E., Wheatley, V., Smart, M. K., Petty, D. J., & Basore, K. D., *Flow physics inside a shape-transitioning scramjet engine*, 18th AIAA/3AF ISPHSTC, 24-28 September, Tours, France2012.
17) Nompelis, I., Drayna, T. W. & Candler, G. V., *Development of a Hybrid Unstructured Implicit Solver for the Simulation of Reacting Flows Over Complex Geometries*, 34th AIAA Fluid Dynamics Conference and Exhibit, 2004, Portland, Oregon.
18) Wright, M J., Candler, G. V. & Bose, D., *Data-Parallel Line Relaxation Method for the Navier-Stokes Equations*, AIAA Journal, 36, No.9, 1998, 1603-1609.
19) Pangedarm, H. G., Seitz, G., *An algorithm for detection and visualization of discontinuities in scientific data fields applied to flow data with shock waves* III. Eurographics Workshop in Visualization in Scientific Computing, Viareggio, Italy, 1992 27-29.
20) Fritsch, F. N. & Carlson R. E., *Monotone Piecewise Cubic Interpolation*, SIAM J. Numerical Analysis, 17, 1980, 238-246.
21) Wise, D., *Experimental Investigation of a 3D Scramjet Engine at Hypervelocity Conditions*, PhD Thesis, The University of Queensland, 2014.